

Energy Bounds from Relative Magnetic Helicity in Spherical Shells

ANTHONY R. YEATES  AND GUNNAR HORNIG ¹*Department of Mathematical Sciences, Durham University, Durham, DH1 3LE, UK*²*Division of Mathematics, University of Dundee, Dundee, DD1 4HN, UK*

(Accepted December 23, 2025)

Submitted to ApJ

ABSTRACT

Relative magnetic helicity is commonly used in solar physics to avoid the well known gauge ambiguity of standard magnetic helicity in magnetically open domains. But its physical interpretation is difficult owing to the invocation of a reference field. For the specific case of spherical shell domains (with potential reference field), relative helicity may be written intrinsically in terms of the magnetic field alone, without the need to calculate the reference field or its vector potential. We use this intrinsic expression to prove that non-zero relative helicity implies lower bounds for both magnetic energy and free magnetic energy, generalizing the important Arnol'd inequality known for closed-field magnetic helicity. Further, we derive a stronger energy bound by spatially decomposing the relative helicity over a magnetic partition of the domain to obtain a new ideal invariant which we call unsigned helicity. The bounds are illustrated with analytical linear force-free fields (that maximize relative helicity for given boundary conditions) as well as a non-potential data-driven model of the solar corona. These bounds confirm that both relative helicity and the unsigned helicity can influence the dynamics in the solar corona.

Keywords: Solar magnetic fields (1503)

1. INTRODUCTION

In solar physics, it is common to avoid gauge ambiguities in the classical magnetic helicity,

$$H = \int_V \mathbf{A} \cdot \mathbf{B} \, dV, \quad (1)$$

by measuring instead the relative (magnetic) helicity of Berger & Field (1984), which we denote H_R . This is most commonly computed from the Finn & Antonsen (1985) formula,

$$H_R = \int_V (\mathbf{A} + \mathbf{A}_p) \cdot (\mathbf{B} - \mathbf{B}_p) \, dV, \quad (2)$$

where $\mathbf{B} = \nabla \times \mathbf{A}$ is the magnetic field of interest, and $\mathbf{B}_p = \nabla \times \mathbf{A}_p$ is a reference field matching $\mathbf{n} \cdot \mathbf{B}_p|_{\partial V} = \mathbf{n} \cdot \mathbf{B}|_{\partial V}$ on the boundary ∂V . Using

(2), the relative helicity is easily shown to be invariant under gauge transformations of either \mathbf{A} or \mathbf{A}_p . It is conserved in ideal magnetohydrodynamics in line-tied situations where $\mathbf{v} = \mathbf{0}$ on ∂V , and – crucially – remains approximately conserved even under magnetic reconnection (Berger 1984; Blackman 2015). We use the notation \mathbf{B}_p because the reference field is almost universally taken to be the unique potential (current-free) field satisfying $\nabla \times \mathbf{B}_p = \mathbf{0}$ in V as well as the boundary matching condition. Among all magnetic fields satisfying these boundary conditions, \mathbf{B}_p is well known to have minimum energy, or in other words to minimize the L^2 -norm $\|\mathbf{B}\|^2 \equiv \int_V |\mathbf{B}|^2 \, dV$. By definition, H_R vanishes if $\mathbf{B} = \mathbf{B}_p$. The relative helicity H_R has been widely used in solar physics to analyze magnetic activity (e.g., Démoulin & Pariat 2009; Toriumi & Wang 2019; Thalmann et al. 2021).

Oddly, much less attention has been paid in the literature to what H_R is actually measuring, and why it can reasonably be expected to give us useful information about the dynamics. In particular, the fact that

H_R is conserved (or approximately conserved) in a line-tying evolution is not in itself a particularly compelling reason to study it, since any choice of classical helicity H is also conserved in such an evolution, provided $\mathbf{n} \times \mathbf{A}|_{\partial V}$ is held fixed over time. Indeed, as long as \mathbf{B} contains at least one open magnetic field line (intersecting ∂V), one can choose the gauge of \mathbf{A} to give H an arbitrary numerical value, of either sign. This value will remain unchanged in the evolution provided that line-tying holds and that the gauge of $\mathbf{n} \times \mathbf{A}|_{\partial V}$ is fixed. Thus although this H is conserved, its numerical value cannot tell us anything about the magnetic field, since it is arbitrary.

By contrast, in the magnetically-closed case, both the sign and magnitude of H are meaningful: it is gauge independent and measures the average pairwise linking between infinitesimal flux tubes within the magnetic field (e.g., Moffatt & Ricca 1992; Berger 1999; Moffatt & Dormy 2019). Moreover, for this case, H is well known to obey an inequality of the form

$$|H| \leq C\|\mathbf{B}\|^2, \quad (3)$$

showing that a non-zero helicity puts a lower bound on the magnetic energy (Arnol'd 1986; Cantarella et al. 2001; Berger 2003). Our main aim in this paper is to show that an analogous inequality holds for H_R , at least when V is a spherical shell (the region between two concentric spheres) and the reference field is potential.

In realistic magnetic fields, the bound $|H|/C$ from (23) can be a significant underestimate for $\|\mathbf{B}\|^2$. For example, it is certainly possible to have $H = 0$ even though the magnetic field has non-trivial topology (e.g., Candelaresi & Brandenburg 2011; Pontin et al. 2016). Stronger energy bounds have been derived in terms of so-called crossing numbers, as reviewed by Berger (2003). These apply to both magnetically-closed knotted fields (Freedman & He 1991) and “braided” fields between two boundaries (Berger 1993; Aly 2014; Yeates et al. 2014). However, these crossing numbers are not conserved in an ideal evolution. In this paper, we focus on obtaining energy inequalities where the left-hand side is also a conserved quantity. This is because our overall aim is not to generate the tightest possible bound on energy for a known magnetic field (indeed, if \mathbf{B} is known then one can compute the energy directly), but to (i) put robust bounds on how energy could evolve, and (ii) show that H_R (and related conserved quantities) can constrain the dynamics. With the crossing number approach, it is a challenging problem to determine the minimum possible energy over all ideally accessible configurations (but see, e.g. Ricca 2013). Instead, we will show (Section 4) how to strengthen the inequality while retaining ideal

invariance of the left-hand side, by partitioning V into magnetic subdomains.

The reason for restricting to a spherical shell is that we can take advantage of poloidal-toroidal decomposition of \mathbf{B} (Backus 1958; Berger 1985). As will be shown in Section 2, the known Green's function expressions for the poloidal and toroidal potentials give us an explicit expression for H_R in terms of \mathbf{B} alone, with no reference to either \mathbf{B}_p or to any vector potentials \mathbf{A} or \mathbf{A}_p . Analogous expressions are available in the planar slab (region between two parallel planes), but in other domains a generalized decomposition is required (Berger & Hornig 2018; Yi & Choe 2022); it is quite possible that H_R may still give a lower bound for $\|\mathbf{B}\|^2$, but our proofs do not apply directly.

In spherical shells, the simplification of H_R has previously been exploited to relate energy to helicity for the specific case of force-free fields (up to a boundary term; Berger 1988), to interpret H_R as a sum of pairwise linking between elementary (open-ended) flux tubes (Demoulin et al. 2006), and to relate helicity to pairwise winding numbers between field lines (Xiao et al. 2023). The latter two works provide physical interpretations of H_R without recourse either to the reference field \mathbf{B}_p , or to fields external to V (unlike Berger & Field 1984; Schuck & Linton 2024). This paper will provide further “intrinsic” evidence for the dynamical significance of H_R in spherical shells.

The paper is organized as follows. Section 2 reviews the fundamental expression for H_R on a spherical shell, on which the rest of the paper is based. The main inequality giving $|H_R| \leq C\|\mathbf{B}\|^2$ is presented in Section 3, where we also obtain an analogous bound replacing $\|\mathbf{B}\|^2$ by free magnetic energy $\|\mathbf{B} - \mathbf{B}_p\|^2$. Section 4 then derives the improved, partition-based bound for $\|\mathbf{B}\|^2$ where H_R is replaced by so-called “unsigned helicity”. The utility of this improved bound is illustrated in Section 5 using a numerical model of the solar corona, with conclusions in Section 6.

2. SPHERICAL SHELLS

In this paper, V denotes a spherical shell with radius $r \in [r_0, r_1]$. The spherical surfaces of constant r are labelled S_r , with $S_0 \equiv S_{r_0}$ denoting the inner boundary and $S_1 \equiv S_{r_1}$ the outer boundary. We assume no net magnetic flux or current through S_r for any $r \in [r_0, r_1]$, meaning

$$\oint_{S_r} \mathbf{e}_r \cdot \mathbf{B} dS = \oint_{S_r} \mathbf{e}_r \cdot \nabla \times \mathbf{B} dS = 0. \quad (4)$$

2.1. Poloidal-Toroidal Vector Potential

In our spherical shell with (4), we can write $\mathbf{B} = \nabla \times \mathbf{A}^*$ where

$$\mathbf{A}^* = \nabla \times (P\mathbf{e}_r) + T\mathbf{e}_r, \quad (5)$$

which is the well-known poloidal-toroidal decomposition of \mathbf{B} (Backus 1958), discussed in the helicity context by Berger (1985) and Berger & Hornig (2018).

To see that \mathbf{A}^* exists, note that taking the curl of (5) once or twice gives

$$\nabla_h^2 P = -\mathbf{e}_r \cdot \mathbf{B}, \quad (6)$$

$$\nabla_h^2 T = -\mathbf{e}_r \cdot \nabla \times \mathbf{B}, \quad (7)$$

on each S_r , in terms of the surface Laplacian

$$\nabla_h^2 \equiv \frac{1}{r^2 \sin \theta} \left[\frac{\partial}{\partial \theta} \left(\sin \theta \frac{\partial}{\partial \theta} \right) + \frac{1}{\sin \theta} \frac{\partial^2}{\partial \phi^2} \right]. \quad (8)$$

These two Poisson equations are solvable for P and T thanks to our assumptions (4). Note that the solutions are unique only up to additive functions of r . Neither of these ambiguities affect H_R , however changing T does change \mathbf{A}^* . To derive our results in Section 2.3 and beyond, we will need to fix \mathbf{A}^* by choosing the particular T with

$$\oint_{S_r} T dS = 0 \quad \text{for each } r \in [r_0, r_1]. \quad (9)$$

2.2. Simple Expression for Relative Helicity

It is known that the expression (2) for H_R simplifies considerably in our spherical shell geometry (Berger 1988; DeVore 2000; Démoulin 2007). To see this, note that applying the equivalent decomposition (5) to the reference vector potential gives $\mathbf{A}_p^* = \nabla \times (P_p \mathbf{e}_r)$, because $\nabla \times \mathbf{B}_p = \mathbf{0}$. Then integrating by parts gives

$$\int_V \mathbf{A}_p^* \cdot \mathbf{B}_p dV = \int_V \mathbf{B}_p \cdot \nabla \times (P_p \mathbf{e}_r) dV = 0. \quad (10)$$

From (2), this leaves

$$H_R = \int_V \mathbf{A}^* \cdot \mathbf{B} dV + \int_V (\mathbf{A}_p^* \cdot \mathbf{B} - \mathbf{A}^* \cdot \mathbf{B}_p) dV \quad (11)$$

$$= \int_V \mathbf{A}^* \cdot \mathbf{B} dV + \oint_{\partial V} \mathbf{n} \cdot (\mathbf{A}^* \times \mathbf{A}_p^*) dS. \quad (12)$$

But since P and P_p both solve the same Poisson equation (6), they can differ only by an additive constant on each of S_0 , S_1 , so that the boundary integral vanishes. Therefore

$$H_R = \int_V \mathbf{A}^* \cdot \mathbf{B} dV. \quad (13)$$

In other words, for the spherical shell, H_R is equivalent to H in the poloidal-toroidal gauge. Note that this expression holds for any choice of T . It is the starting point for the energy bounds derived in this paper, for which we will use the particular choice (9) for T .

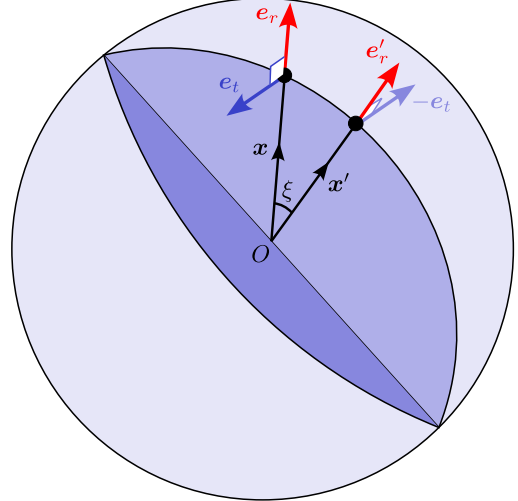


Figure 1. Geometry for Sections 2.3 and 2.4 – in particular, the intrinsic expression (20) for H_R . Note that $\mathbf{x} = r\mathbf{e}_r$ and $\mathbf{x}' = r\mathbf{e}'_r$.

2.3. Intrinsic Expression for \mathbf{A}_p^*

To derive our energy bounds, we will express \mathbf{A}^* in terms of \mathbf{B} . This can be done using Green's functions to write the solutions to (6) and (7) as

$$P(\mathbf{x}) = - \int_{S_r'} (\mathbf{e}'_r \cdot \mathbf{B})(\mathbf{x}') G(\mathbf{x}, \mathbf{x}') dS', \quad (14)$$

$$T(\mathbf{x}) = - \int_{S_r'} (\mathbf{e}'_r \cdot \nabla' \times \mathbf{B})(\mathbf{x}') G(\mathbf{x}, \mathbf{x}') dS'. \quad (15)$$

Here $\mathbf{x} = r\mathbf{e}_r$ and $\mathbf{x}' = r\mathbf{e}'_r$ are points on the sphere S_r and the spherical Green's function is

$$G(\mathbf{x}, \mathbf{x}') = \frac{1}{4\pi} \log(1 - \cos \xi), \quad (16)$$

with ξ the angle between \mathbf{x} and \mathbf{x}' (see Figure 1). The particular solutions (14) and (15) both have zero mean on every S_r (e.g. Backus 1958), so in particular (15) satisfies (9). Substituting into (5) gives

$$\begin{aligned} \mathbf{A}^*(\mathbf{x}) &= \mathbf{e}_r \times \left(\int_{S_r'} B_r(\mathbf{x}') \nabla_h G dS' \right) \\ &+ \left(\int_{S_r'} \mathbf{B}(\mathbf{x}') \cdot \mathbf{e}'_r \times \nabla'_h G dS' \right) \mathbf{e}_r. \end{aligned} \quad (17)$$

As observed by Xiao et al. (2023), we have

$$\mathbf{e}_r \times \nabla_h G = \frac{\mathbf{x}' \times \mathbf{x}}{4\pi r^3 (1 - \cos \xi)}, \quad (18)$$

and $\mathbf{e}'_r \times \nabla'_h G = -\mathbf{e}_r \times \nabla_h G$.

2.4. Intrinsic Expression for H_R

As an aside, we can use (17) to derive a new expression for H_R . Following Xiao et al. (2023), we define the unit vector

$$\mathbf{e}_t = \frac{\mathbf{x}' \times \mathbf{x}}{|\mathbf{x}' \times \mathbf{x}|} = \frac{\mathbf{x}' \times \mathbf{x}}{r^2 \sin \xi}, \quad (19)$$

which is orthogonal to the great circle connecting \mathbf{x} and \mathbf{x}' (Figure 1). Substituting (17) into (13) and defining $\Gamma(\xi) = \sin \xi / (1 - \cos \xi)$ leads to the alternative expression

$$H_R = \int_{r_0}^{r_1} \int_{S_r \times S'_r} \frac{\Gamma(\xi)}{4\pi r} \left[B_r(\mathbf{x}') B_t(\mathbf{x}) - B_r(\mathbf{x}) B_t(\mathbf{x}') \right] dS' dS dr, \quad (20)$$

where $B_t \equiv \mathbf{B} \cdot \mathbf{e}_t$. Note that $\Gamma(\xi)$ has a singularity when $\mathbf{x}' = \mathbf{x}$, since $\sin \xi / (1 - \cos \xi) \sim 2/\xi$ as $\xi \rightarrow 0$. However, choosing coordinates for S' where \mathbf{x} is the north pole makes ξ into colatitude, so the surface element dS' contributes another $\sin \xi$, showing that the integrand remains finite. Expression (20) is “intrinsic” in the sense that it refers to neither any vector potential nor any reference field.

From Figure 1, we see that $B_t(\mathbf{x})$ is the component of $\mathbf{B}(\mathbf{x})$ “rotating around” \mathbf{x}' , and *vice versa* for $B_t(\mathbf{x}')$. So (20) has the clear interpretation of measuring the average winding of \mathbf{B} between all pairs of points, with respect to the radial direction. Xiao et al. (2023) show that the weighting $\Gamma(\xi)$ accounts naturally for the spherical geometry; this factor vanishes when $\xi = \pi$, meaning \mathbf{x} and \mathbf{x}' are antipodal. By recasting (20) as an integral over field lines rather than height, they also show how to express H_R in a spherical shell as a flux-weighted average of pairwise winding numbers between magnetic field lines. This is analogous to the topological interpretation of H in terms of linking numbers.

We could also view the expression (20) for H_R as a two-point correlation function for \mathbf{B} , using off-diagonal components of the tensor $B_i B_j$. This is reminiscent of the well-known interpretation for H in periodic domains (using Coulomb gauge, $\nabla \cdot \mathbf{A}^c = 0$), used to evaluate helicity in studies of solar wind turbulence (Matthaeus & Goldstein 1982; Narita 2024).

3. GLOBAL ENERGY BOUNDS

In Section 3.1 we generalize the Arnold (1986) inequality (23) to H_R , for a spherical shell. Before doing so, recall the typical proof for (23) in a magnetically closed domain. This starts from the Cauchy-Schwartz inequality

$$\left| \int_V \mathbf{A} \cdot \mathbf{B} dV \right| \leq \int_V |\mathbf{A} \cdot \mathbf{B}| dV \leq \|\mathbf{A}\| \|\mathbf{B}\|, \quad (21)$$

where $\|\cdot\|^2 = \int_V |\cdot|^2 dV$ denotes the L^2 -norm of a vector field on V . Inequality (21) holds in any gauge, but since the helicity is gauge independent in such a domain, we are free to choose a gauge where \mathbf{A} obeys a Poincaré inequality

$$\|\mathbf{A}\| \leq C \|\mathbf{B}\| \quad (22)$$

for some fixed constant C . For example, in a magnetically closed domain such an inequality is satisfied by the Coulomb gauge \mathbf{A}^c with $\nabla \cdot \mathbf{A}^c = 0$ in V and $\mathbf{n} \cdot \mathbf{A}^c = 0$ on ∂V (e.g. Yoshida & Giga 1990). Then we obtain the desired energy bound

$$\left| \int_V \mathbf{A} \cdot \mathbf{B} dV \right| \leq C \|\mathbf{B}\|^2. \quad (23)$$

Next consider our magnetically-open spherical shell.

3.1. Lower Bound for Energy

For H_R , we are no longer free to choose the vector potential in (1), but must verify (22) for our particular gauge \mathbf{A}^* from (5) and (9). We find that this can be done using the integral expression (17) for \mathbf{A}^* in terms of \mathbf{B} alone, by adapting the argument of Cantarella et al. (2001). As detailed in Appendix A, this leads to

$$\|\mathbf{A}^*\| \leq \frac{\pi r_1}{2} \|\mathbf{B}\|, \quad (24)$$

and hence (21) gives

$$|H_R| \leq \frac{\pi r_1}{2} \|\mathbf{B}\|^2, \quad (25)$$

or equivalently the energy bound

$$\|\mathbf{B}\|^2 \geq W_1 \equiv \frac{2|H_R|}{\pi r_1} \quad (26)$$

for our spherical shell.

The bound (26) is not tight, in the sense that equality may be impossible to attain for any \mathbf{B} , at least for certain boundary conditions. To see this, note first that a magnetic field that maximizes the ratio $W_1 / \|\mathbf{B}\|^2$ – in other words, maximizes the tightness of the bound – must be a linear force-free field satisfying

$$\nabla \times \mathbf{B} = \alpha \mathbf{B}, \quad \alpha = \text{constant}. \quad (27)$$

This follows from Woltjer’s Theorem (Woltjer 1958), as extended by Berger (1984) to the case of H_R with fixed $B_r|_{\partial V}$ (we give an alternative proof in Appendix B using \mathbf{A}^*).

Then consider a simple example where we fix B_r on both boundaries to match the dipolar “source surface” potential field,

$$\mathbf{B}_p = B_0 \left[\frac{r_0^3(r^3 + 2r_1^3)}{r^3(r_0^3 + 2r_1^3)} \cos \theta \mathbf{e}_r - \frac{r_0^3(r^3 - r_1^3)}{r^3(r_0^3 + 2r_1^3)} \sin \theta \mathbf{e}_\theta \right]. \quad (28)$$

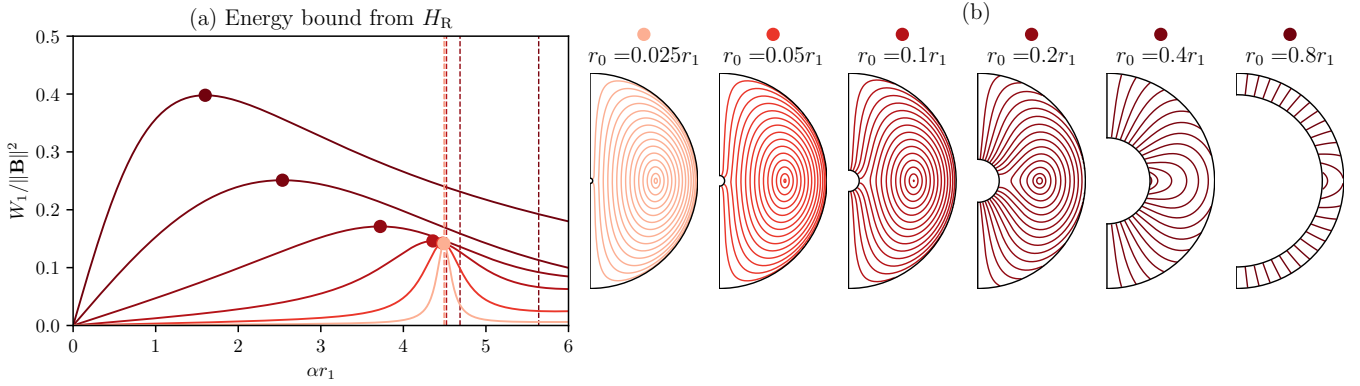


Figure 2. Linear force-free fields matching B_r from (28) on both S_0 and S_1 . Panel (a) shows the ratio $W_1/\|\mathbf{B}\|^2$ in energy bound (26) for these fields, as a function of (normalized) α . Curves represent domains with different r_0/r_1 , with colored dots showing the maximizing solution in each case. Panel (b) shows the flux surfaces for these maximizing solutions. Dashed vertical lines in (a) show the lowest resonant values of α (Appendix C).

(This is the unique curl-free field with $B_r = B_0 \cos \theta$ on S_0 that is purely radial on S_1 .) There is a whole family of linear force-free fields with B_r matching (28) on both boundaries, having different values of α (details in Appendix C), and different values of the ratio $W_1/\|\mathbf{B}\|^2$. This ratio is plotted in Figure 2(a) as a function of (non-dimensionalized) αr_1 , with each curve corresponding to a different ratio r_0/r_1 for the domain. For any αr_1 , the ratio $W_1/\|\mathbf{B}\|^2$ for these linear force-free fields depends only on the “shape” r_0/r_1 of the domain, and not the absolute “size” r_1 . The dots indicate the solution that maximizes $W_1/\|\mathbf{B}\|^2$ for each domain shape, and the field line topology of each of these solutions is indicated in Figure 2(b). Here the contours show surfaces of constant $rR(r) \sin^2 \theta$, where $R(r)$ is defined in Appendix C. These are flux surfaces (tangent to \mathbf{B}) in these axisymmetric fields. Notice that the topology of the maximal-helicity solution changes depending on the domain: it is a sheared arcade for $r_0 = 0.8r_1$, but contains a disconnected “flux rope” when r_0 is small enough.

Returning to the tightness of the bound (26), we see from Figure 2(a) that it is tightest – meaning largest ratio $W_1/\|\mathbf{B}\|^2$ – for larger r_0/r_1 , but for the thinnest shell illustrated ($r_0 = 0.8r_1$), we reach only $W_1 \approx 0.4\|\mathbf{B}\|^2$ for the maximal-helicity solution. Conversely, as $r_0 \rightarrow 0$, the maximal ratio tends to a limit of $W_1 \approx 0.14\|\mathbf{B}\|^2$. In this limit, the corresponding αr_1 converges to the smallest curl eigenvalue for a unit ball, which is approximately 4.4934 (Cantarella et al. 2000, Table I). For non-zero r_0 , the ratio that is possible to attain will depend on the boundary conditions for B_r ; more realistic configurations for the Sun will be considered in Section 5.

3.2. Lower Bound for Free Energy

Since $H_R = 0$ for a potential field, one might suspect that having a non-zero H_R might imply not only a

minimum amount of (total) magnetic energy, $\|\mathbf{B}\|^2$, as shown in (26), but also some minimum amount of free magnetic energy, $\|\mathbf{B}_J\|^2$, where

$$\|\mathbf{B}_J\|^2 = \|\mathbf{B} - \mathbf{B}_p\|^2 = \|\mathbf{B}\|^2 - \|\mathbf{B}_p\|^2. \quad (29)$$

Here we prove this for our spherical shell.

To derive a bound for $\|\mathbf{B}_J\|^2$ in terms of H_R , we recall the decomposition

$$H_R = H_J + H_{PJ}, \quad (30)$$

where the two terms

$$H_J = \int_V \mathbf{A}_J \cdot \mathbf{B}_J dV, \quad H_{PJ} = 2 \int_V \mathbf{A}_p \cdot \mathbf{B}_J dV \quad (31)$$

are individually gauge invariant (Berger 1999). They have been called the “current-carrying” and “volume-threading” helicities, respectively (Linan et al. 2018). Choosing $\mathbf{A}_J = \mathbf{A}_J^*$ allows us to immediately apply (26) to \mathbf{B}_J to see that

$$|H_J| \leq \frac{\pi r_1}{2} \|\mathbf{B}_J\|^2. \quad (32)$$

This already gives us the free energy bound

$$\|\mathbf{B}_J\|^2 \geq W_2 \equiv \frac{2|H_J|}{\pi r_1}, \quad (33)$$

but this only implies non-zero free energy in magnetic fields with non-zero H_J .

To go further, we can bound H_{PJ} by

$$|H_{PJ}| \leq 2 \int_V |\mathbf{A}_p| |\mathbf{B}_J| dV \leq 2 \|\mathbf{A}_p\| \|\mathbf{B}_J\|. \quad (34)$$

Choosing $\mathbf{A}_p = \mathbf{A}_p^*$ shows from (24) that

$$\|\mathbf{A}_p^*\| \leq \frac{\pi r_1}{2} \|\mathbf{B}_p\| \quad (35)$$

and so combining we obtain the inequality

$$|H_R| \leq \frac{\pi r_1}{2} \left(\|\mathbf{B}_J\|^2 + 2\|\mathbf{B}_p\| \|\mathbf{B}_J\| \right). \quad (36)$$

MacTaggart (2025) has recently published a tighter inequality of the same form, in the sense that the coefficient of $\|\mathbf{B}_J\|^2$ is smaller – this is derived by noting that \mathbf{B}_J is a closed magnetic field so that the estimate (32) can be replaced by the classical bound (23).

Note the appearance of $\|\mathbf{B}_p\|$ on the right-hand side of (36). We could not expect to bound $|H_R|$ in terms of $\|\mathbf{B}_J\|$ alone, since in configurations where \mathbf{B}_J and \mathbf{B}_p are interlinked, it is possible to increase $|H_R|$ without bound by increasing the strength of \mathbf{B}_p while keeping \mathbf{B}_J fixed. A simple example of this is the linear combination of a dipole and a toroidal field,

$$\mathbf{B} = ar_0^3 \left(\frac{2\cos\theta}{r^3} \mathbf{e}_r + \frac{\sin\theta}{r^3} \mathbf{e}_\theta \right) + \frac{br}{r_0} \sin\theta \mathbf{e}_\phi. \quad (37)$$

Here \mathbf{B}_J is precisely the ϕ -component, and it is straightforward to show that

$$\mathbf{A}^* = \frac{br^2}{r_0} \cos\theta \mathbf{e}_r + \frac{ar_0^3}{r^2} \sin\theta \mathbf{e}_\phi \quad (38)$$

so that

$$H_R = \frac{8\pi abr_0^4}{3} \left(\frac{r_1^2}{r_0^2} - 1 \right). \quad (39)$$

We see that indeed H_R can be increased arbitrarily by increasing the amplitude a of the \mathbf{B}_p component, while holding b fixed so that \mathbf{B}_J is unchanged.

By elementary calculus, we can solve (36) for $\|\mathbf{B}_J\|$ to see that

$$\|\mathbf{B}_J\| \geq \|\mathbf{B}_p\| \left(\sqrt{1 + \frac{2|H_R|}{\pi r_1 \|\mathbf{B}_p\|^2}} - 1 \right), \quad (40)$$

and squaring gives the desired bound

$$\|\mathbf{B}_J\|^2 \geq W_3 \quad (41)$$

for

$$W_3 \equiv \frac{2|H_R|}{\pi r_1} + 2\|\mathbf{B}_p\|^2 \left(1 - \sqrt{1 + \frac{2|H_R|}{\pi r_1 \|\mathbf{B}_p\|^2}} \right). \quad (42)$$

Observe that if \mathbf{B}_p vanishes so that $\mathbf{B} \equiv \mathbf{B}_J$, then $H_R \equiv H_J$ and (41) reduces to (33). Also, W_3 is always non-negative: this can be seen from (40).

Figure 3 explores the tightness of the bounds (33) and (41) for the same dipolar linear force-free configurations as in Figure 2. The dots in this figure again correspond to the maximizers of $|H_R|/\|\mathbf{B}\|^2$. Figure

3(a) shows that, for these maximizers, a greater proportion of $\|\mathbf{B}\|^2$ comes from $\|\mathbf{B}_J\|^2$ as $r_0 \rightarrow 0$. Indeed, for the cases with $r_0 \leq 0.1r_1$, $\|\mathbf{B}_p\|^2$ is negligible. This is seen indirectly by how the flux surfaces in Figure 2 become “almost closed” and barely affected by the open boundary conditions for small r_0 . Correspondingly, as r_0 decreases, more and more of H_R comes from H_J , as shown in Figure 3(b). As a result, as $r_0 \rightarrow 0$, the tightness of the bound (33) in Figure 3(c), becomes equivalent to that of the original bound (26) in Figure 2(b), with $W_2 \approx 0.14\|\mathbf{B}_J\|^2$. On the other hand, for the thinnest shell $r_0 = 0.8r_1$, we see from Figure 3(b) that $H_R \approx H_{PJ}$, so that $W_2/\|\mathbf{B}_J\|^2 \rightarrow 0$ and the bound (33) becomes useless, even though $\|\mathbf{B}_J\|^2$ is still about half of $\|\mathbf{B}\|^2$.

By contrast, the tightness of the energy bound (41) for the linear force-free maximizers shows a non-monotonic dependence on α (Figure 3d). Notably, it is bounded away from zero for all r_0 , so that non-zero free energy is guaranteed whether H_R is coming predominantly from H_J or H_{PJ} , or from a mixture. On the other hand, for small r_0 the H_R -based bound W_3 does not become independent of r_0 , and remains slightly lower than W_2 at $r_0 = 0.025r_1$, even though $\|\mathbf{B}_p\|^2$ is negligible compared to $\|\mathbf{B}_J\|^2$.

4. LOCAL ENERGY BOUNDS

The bounds derived in Section 3 have been based on the global H_R value, integrated over the whole of V . Here, we spatially decompose H_R into a sum over more localized invariants, leading to stronger energy bounds. It would, of course, be possible to bound $\|\mathbf{B}\|^2$ based on $\int_V \mathbf{A}^* \cdot \mathbf{B} dV$ directly, bypassing the first inequality in (21). However, this integral is not an ideal invariant, and we prefer to bound the energy in terms of a conserved quantity that is likely to be more robust in simulation or measurement. To achieve this, we need to decompose H_R not into arbitrary volumes (cf. Valori et al. 2020), but into subdomains separated by magnetic surfaces.

4.1. Partitioning the Domain

The expression (13) suggests – unlike the Finn-Antonsen formula (2) – how to spatially decompose H_R into a sum of more localized “sub-helicities”,

$$H_R = \sum_{V_i \in \Pi} h_i, \text{ where } h_i = \int_{V_i} \mathbf{A}^* \cdot \mathbf{B} dV, \quad (43)$$

where $\Pi = \{V_i\}$ is a disjoint partition of V , meaning $V = \bigcup_i V_i$ and $V_i \cap V_j = 0$ for $i \neq j$. For an arbitrary such partition, each h_i may not be an ideal invariant. But if the V_i are magnetic subvolumes – meaning that $\mathbf{B} \cdot \mathbf{n}_i = 0$ on the part of ∂V_i that is internal to the

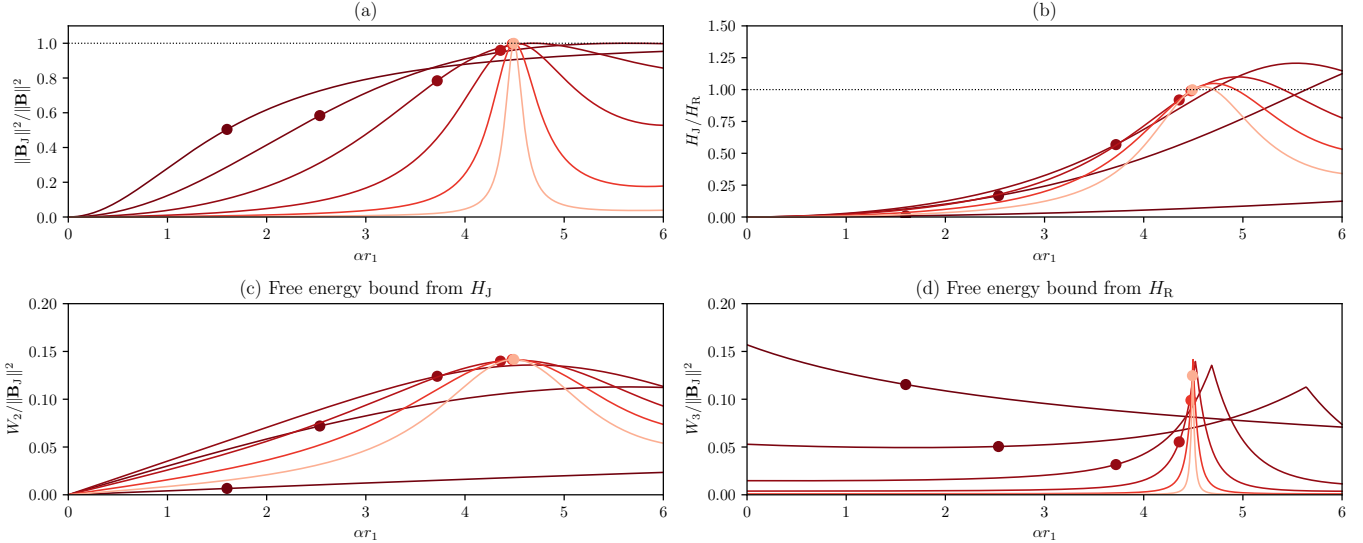


Figure 3. Normalized (a) free energy $\|\mathbf{B}_J\|^2$ and (b) current-carrying helicity H_J , for the linear force-free solutions in Figure 2. Panels (c) and (d) show the ratios $W_2/\|\mathbf{B}_J\|^2$ and $W_3/\|\mathbf{B}_J\|^2$ in energy bounds (33) and (41), respectively. Curves represent the same domains (r_0/r_1) as Figure 2, and colored dots all show the fields maximizing the original bound $W_1/\|\mathbf{B}\|^2$.

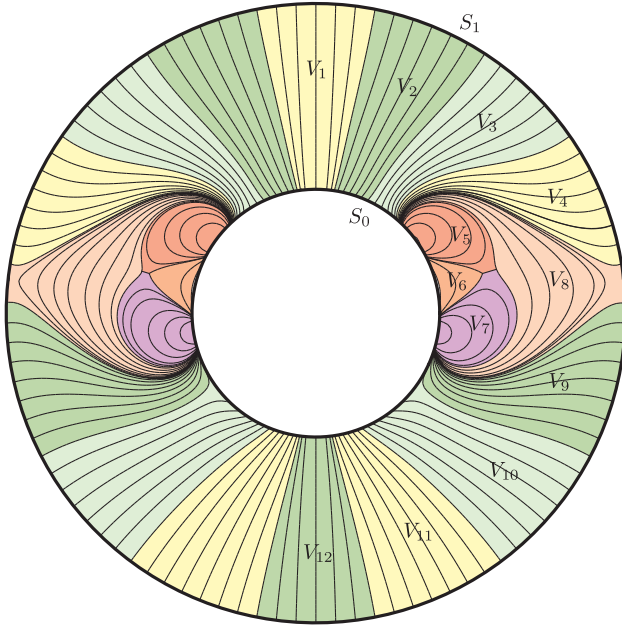


Figure 4. An example partition Π of the spherical shell V into magnetic subvolumes V_1, \dots, V_{12} , in this case for an axisymmetric magnetic field. Each subvolume V_i has an associated sub-helicity, h_i , with $\sum_{i=1}^{12} h_i = H_R$.

overall V – then the Reynolds Transport Theorem (e.g. Moffatt & Dormy 2019), with the uncurred ideal induction equation

$$\frac{\partial \mathbf{A}^*}{\partial t} = \mathbf{v} \times \mathbf{B} + \nabla \phi^*, \quad (44)$$

gives

$$\frac{dh_i}{dt} = \oint_{\partial V_i \cap \partial V} (\phi^* + \mathbf{A}^* \cdot \mathbf{v}) \mathbf{B} \cdot d\mathbf{S}. \quad (45)$$

With the global line-tied boundary condition $\mathbf{v}|_{\partial V} = \mathbf{0}$, the second term in the parentheses vanishes, and it follows also that $\nabla_h \phi^*|_{\partial V} = 0$. This means that we can take ϕ^* outside the integral on each boundary surface S_0 and S_1 , so by (4) we have

$$\frac{dh_i}{dt} = 0. \quad (46)$$

In other words, each sub-helicity is invariant under ideal motions that vanish on the global boundaries. Thus we have decomposed H_R into more localized invariants, albeit that the computation of \mathbf{A}^* is defined globally. An example of such a partition is shown in Figure 4.

4.2. Bound from a Magnetic Partition

We can exploit the partition (43) to give a stronger lower bound on the magnetic energy. To do this, define the unsigned helicity of the partition as

$$\overline{H}_\Pi = \sum_{V_i \in \Pi} |h_i|. \quad (47)$$

This is, again, an ideal invariant provided the V_i are magnetic subvolumes. It satisfies

$$\overline{H}_\Pi = \sum_{V_i \in \Pi} \left| \int_{V_i} \mathbf{A}^* \cdot \mathbf{B} dV \right| \quad (48)$$

$$\leq \sum_{V_i \in \Pi} \int_{V_i} |\mathbf{A}^* \cdot \mathbf{B}| dV = \int_V |\mathbf{A}^* \cdot \mathbf{B}| dV. \quad (49)$$

This recovers (21), so it follows from Section 3 that \bar{H}_Π for any disjoint partition Π also obeys

$$\bar{H}_\Pi \leq \frac{\pi r_1}{2} \|\mathbf{B}\|^2. \quad (50)$$

For the Sun’s corona, where there are positive and negative regions of helicity, a fine enough choice of partition will typically give a larger lower bound on the energy than (26).

4.3. Bound From Field Line Helicity

To obtain the tightest possible bound for $\|\mathbf{B}\|^2$ using (50), we seek the finest possible partition Π . This is given by taking each V_i to be a thin flux tube around a single magnetic field line L_i , and taking the limit that these tube radii $r(V_i)$ go to zero. Since h_i would vanish in this limit, we normalize by the tube’s magnetic flux Φ_i to obtain a finite value

$$\mathcal{A}(L_i) = \lim_{r(V_i) \rightarrow 0} \frac{1}{\Phi_i} \int_{V_i} \mathbf{A}^* \cdot \mathbf{B} dV. \quad (51)$$

Called field line helicity (Yeates & Berger 2024), it was shown by Berger (1988) showed that this quantity has the simpler expression

$$\mathcal{A}(L_i) = \int_{L_i} \mathbf{A}^* \cdot d\mathbf{l}. \quad (52)$$

Again, this is invariant for every field line under a line-tied ideal evolution. For a closed loop field line, $\mathcal{A}(L_i)$ is simply the enclosed magnetic flux. For an open field line, it still corresponds to a flux, although the interpretation is more nuanced (e.g., Yeates & Hornig 2016). We recover H_R by replacing the sum in (43) by an integral of $\mathcal{A}(L_i)d\Phi_i$ over all field lines. In the (typical) case where all field lines intersect ∂V exactly twice, this may be written as

$$H_R = \frac{1}{2} \oint_{\partial V} \mathcal{A} |B_r| dS, \quad (53)$$

where \mathcal{A} is integrated along the field line traced from each point on ∂V .

The corresponding unsigned helicity of this limiting “field line” partition is similarly given by replacing the sum in (47) with an integral, so that

$$\bar{H} = \frac{1}{2} \oint_{\partial V} |\mathcal{A} B_r| dS. \quad (54)$$

This was called “unsigned helicity” by Yeates (2020). From (50) this again obeys the inequality

$$\bar{H} \leq \frac{\pi r_1}{2} \|\mathbf{B}\|^2. \quad (55)$$

Since this is the finest possible (magnetic) partition, it gives us the tightest possible energy bound from the partition approach, namely

$$\|\mathbf{B}\|^2 \geq W_4 = \frac{2\bar{H}}{\pi r_1}. \quad (56)$$

It is clear that (56) will reduce to the original bound (26) precisely when $\bar{H} = H_R$. This occurs when \mathcal{A} either vanishes or has uniform sign for all field lines. It is not so common for \mathcal{A} to vanish uniformly: as shown by Yeates (2020), even (non-axisymmetric) potential fields typically have non-zero \mathcal{A} values on individual field lines. But the second case – uniform sign of \mathcal{A} – can occur, at least in artificial configurations. An example is the family of linear force-free fields from Section 3 (Appendix C). Bound (56) therefore gives no new information for these fields. On the other hand, the more typical situation in the solar corona is to have mixed signs of \mathcal{A} , in which case $\bar{H} > H_R$ (e.g., Yeates 2024) and bound (56) constrains $\|\mathbf{B}\|^2$ more strongly. This will be illustrated in the following section.

5. NUMERICAL EXAMPLE

It is clear from observations that the real solar corona does not resemble the maximal helicity fields illustrated in Figure 2 (Pevtsov & Balasubramaniam 2003; Pevtsov et al. 2014). In particular, there are sub-regions of both positive and negative (field line) helicity, as well as regions – particularly in the open field – where the field lines are likely close to potential (Yeates & Hornig 2016). To capture these general features, we illustrate here some recent magneto-frictional simulations of Solar Cycle 24 by Yeates (2024), although our interest here is purely to get a feeling for what to expect more generally from solar coronal magnetic field models.

5.1. Solar Cycle Simulation

In the numerical simulations by Yeates (2024), the lower boundary, $r_0 = R_\odot$, evolves through a surface flux transport model, and the coronal magnetic field (in $r < r_1 = 2.5R_\odot$) responds by continual relaxation. New active regions are emerged according to SHARP (Spaceweather HMI Active Region Patch) data from Solar Dynamics Observatory (Bobra et al. 2014).

Figure 5 compares two of these simulations with a potential field source surface (PFSS) extrapolation, at a single time near solar maximum. The left column shows magnetic field lines, and the right column shows the distribution of field line helicities on the solar surface (see Appendix D for computational details). As detailed in Yeates (2024), the two simulations have the same B_r on the photosphere, but differ in the helicity of the emerg-

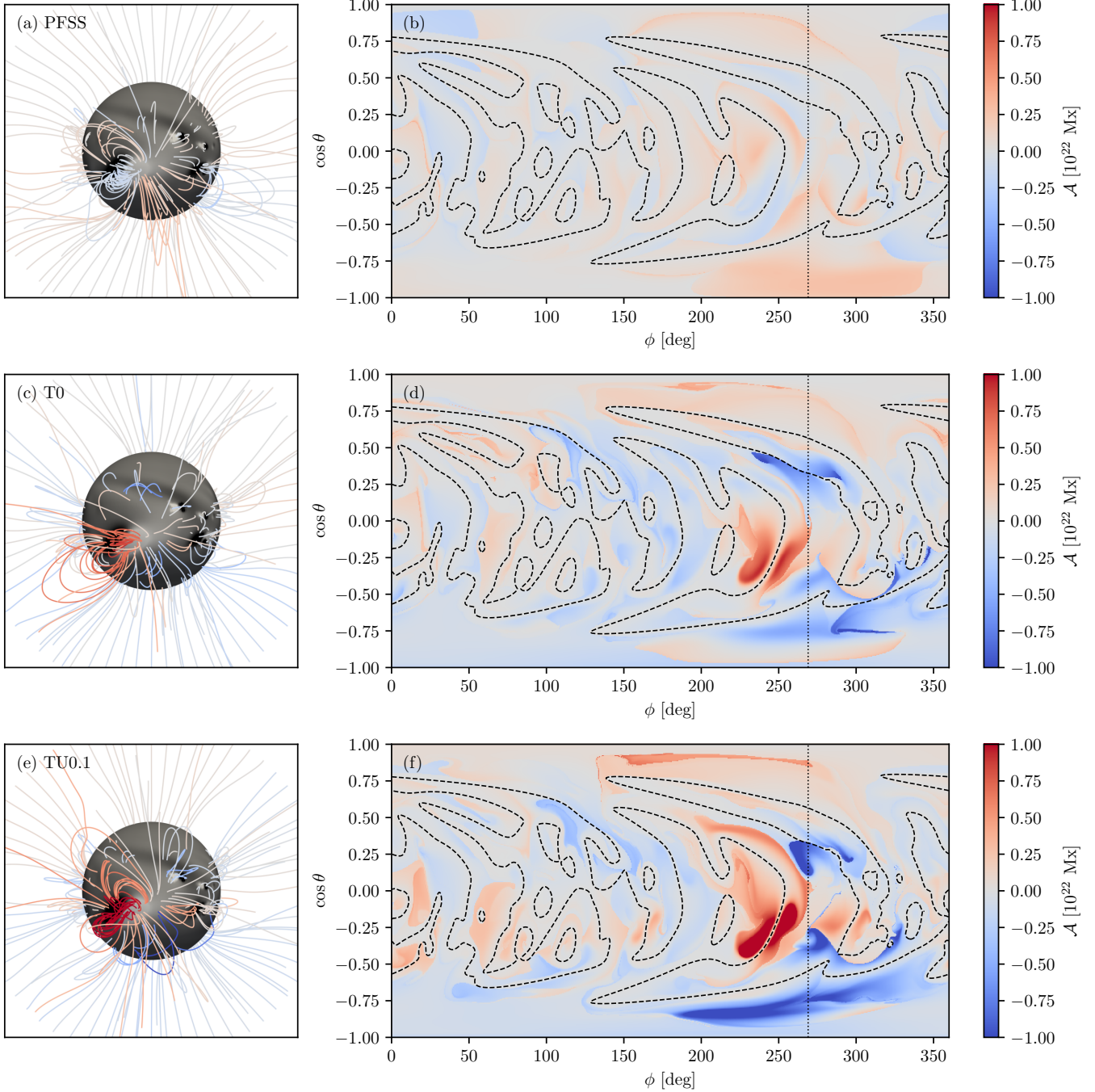


Figure 5. Field line helicity for the same day (2014 December 15) in a PFSS extrapolation (a, b), and two magneto-frictional simulations: T0 (c, d) and TU0.1 (e, f) from [Yeates \(2024\)](#). The right column shows \mathcal{A} as a function of footpoint location on $r = r_0$, with the photospheric neutral line shown dashed. The dotted vertical line shows the longitude of the viewpoint in the left column, where (selected) field lines are shown colored by \mathcal{A} . The color scale is capped at the same value in all plots; actual maxima are $0.4 \times 10^{22} \text{ Mx}$, $1.3 \times 10^{22} \text{ Mx}$ and $3.3 \times 10^{22} \text{ Mx}$.

ing active regions. In run T0, all regions emerge untwisted, so that the helicity is injected primarily through shearing by differential rotation. In run TU0.1, the regions emerge with non-zero helicity that also contributes to the overall helicity in the corona. In both cases, the strongest helicity tends to concentrate in sheared arcades or flux ropes above neutral lines, in what would observationally correspond to filament channels (Martin 1998). In Figures 5(d,f), we see the footpoints of such structures on either side of the neutral lines. Note that, despite having $H_R = 0$, the potential field also contains non-zero field line helicity, as shown in Figure 5(b). This arises from the non-trivial topology of the boundary flux distribution (see Yeates 2020).

5.2. Timeseries

For quantitative comparison, we compute $\|\mathbf{B}\|^2$, $\|\mathbf{B}_J\|^2$, H_R , and \bar{H} from snapshots taken at 27-day intervals in the simulations T0 and TU0.1. Figure 6(a) shows the time variation of $\|\mathbf{B}\|^2$ (multiplied by r_0 to give the same units as helicity) in these two simulations as well as a sequence of corresponding PFSS extrapolations from the (shared) lower boundary distribution. Whilst the PFSS extrapolation is not precisely equal to either of the reference fields \mathbf{B}_p , owing to the different outer boundary condition, its energy is nevertheless a close approximation. Therefore this figure shows that $\|\mathbf{B}_p\|^2$ dominates $\|\mathbf{B}_J\|^2$ throughout these simulations, which is typical for many global coronal models (Yeates et al. 2018).

Figure 6(b) shows how H_R varies between positive and negative, depending on the dominant non-potential structure(s). For example, at the time of the snapshot in Figure 5, we have $H_R > 0$ in both T0 and TU0.1, corresponding to dominance of the large active region around $\cos\theta = -0.25$ and $\phi = 250^\circ$. Although this does not appear to dominate in Figures 5(e) and (f), it does dominate once the flux weighting $|B_r|$ is included in (53). By definition, $H_R = 0$ for the PFSS model, since it is a current-free field. By contrast, the unsigned helicity in Figure 5(c) is always non-negative, shows a more consistent ordering with the value for TU0.1 being larger than for T0, and has a non-zero value (though smaller) for the PFSS model.

5.3. Energy Bounds

The right column of Figure 6 illustrates the tightness of three of the energy bounds from Sections 3 and 4 over the simulations T0 and TU0.1. For the basic bound (26) on $\|\mathbf{B}\|^2$ using $|H_R|$, shown in Figure 6(a), non-zero bounds are obtained whenever $H_R \neq 0$, but note that the ratio $W_1/\|\mathbf{B}\|^2$ is always substantially smaller

than for the linear force-free example in Figure 2. This arises in part from the fact that H_R now incorporates cancelling contributions of positive and negative sign, and in part from the fact that the numerical models are not linear force-free fields and so not maximizers of the ratio. There is a noticeable increase in the ratio after 2018 when H_R becomes uniformly positive, owing to dominance of a particular long-lived structure.

Figure 6(e) shows the ratio $W_3/\|\mathbf{B}_J\|^2$, namely the tightness of the bound (41) on free energy $\|\mathbf{B}_J\|^2$ using H_R and $\|\mathbf{B}_p\|^2$. Whilst this is again non-zero at times where $H_R \neq 0$, the tightness ratio is orders of magnitude lower than the first bound. To understand this behavior of bound (41), divide (42) through by $\|\mathbf{B}_p\|^2$ and set $\varepsilon \equiv W_1/\|\mathbf{B}_p\|^2$. From Figure 6(d), and the fact that $\|\mathbf{B}_J\|^2 < \|\mathbf{B}_p\|^2$, we see that $\varepsilon \ll 1$. Then use Taylor expansion around $\varepsilon = 0$ to see that $W_3 \approx \varepsilon^2 \|\mathbf{B}_p\|^2/4$, so that $W_3/\|\mathbf{B}_J\|^2 \ll \varepsilon$ provided that $\|\mathbf{B}_J\|^2$ is not too small. So the lack of tightness of the free energy bound would seem to be quite a generic situation for global coronal models.

Finally, Figure 6(f) shows the tightness of the improved energy bound (56) on $\|\mathbf{B}\|^2$ based on the unsigned helicity. Overall the ratio $W_4/\|\mathbf{B}\|^2$ is larger than $W_1/\|\mathbf{B}\|^2$, although never exceeding 0.05 (only a fifth of that reached for the maximal helicity linear force-free field in the dipole example with $r_0 = 0.4r_1$). Most significantly, perhaps, this unsigned helicity bound is always non-zero in both runs T0 and TU0.1, unlike the bounds based on H_R . This illustrates how \bar{H} may be better suited than H_R to analyzing these global simulations.

6. CONCLUSION

The bounds derived above show that non-zero relative helicity $|H_R|$ implies non-zero magnetic energy, analogous to classical helicity $|H|$ in a magnetically-closed domain. Similarly, we have shown that non-zero $|H_R|$ implies non-zero *free* magnetic energy. However, just as with H , magnetic fields can put non-trivial topological constraints on the energy even when $H_R = 0$. The unsigned helicity \bar{H} in (54) seems the most natural generalization, and we have shown that if this is non-zero then it implies non-zero magnetic energy even in fields with $H_R = 0$.

In the classical magnetically-closed case, the \mathbf{B} that maximizes helicity for a given magnetic energy depends only on the geometry of the domain (Arnol'd 1986; Cantarella et al. 2001). In the case of H_R , the helicity that can be reached – and nature of the maximizing configuration – depend also on the boundary distribution of $\mathbf{n} \cdot \mathbf{B}$. We illustrated the maximizing \mathbf{B} for the simplest case of a dipole boundary condition, but in future it

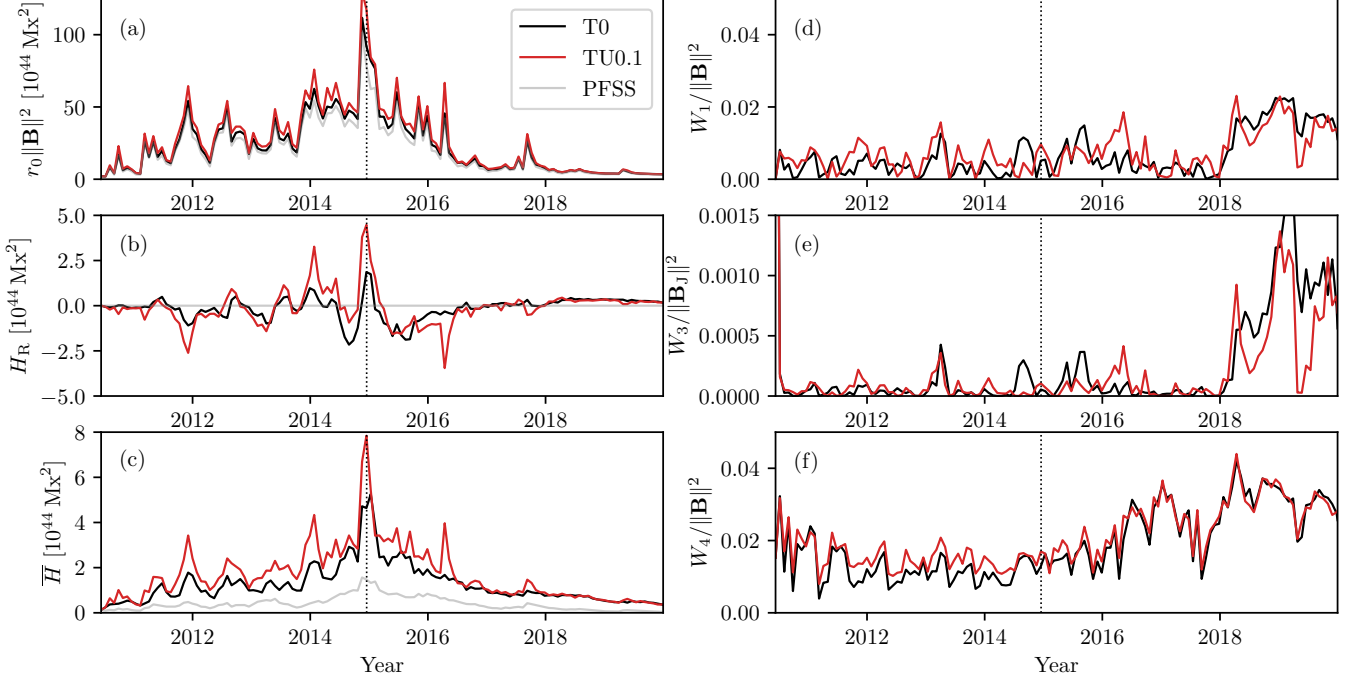


Figure 6. Time series of integrated quantities for the PFSS simulation and two magneto-frictional simulations T0, TU0.1 from Yeates (2024). Left-hand panels show (a) energy $r_0 \|\mathbf{B}\|^2$, (b) relative helicity H_R , and (c) unsigned helicity \bar{H} from equation (47). Right-hand panels (d-f) show the ratios $W_1/\|\mathbf{B}\|^2$, $W_3/\|\mathbf{B}_J\|^2$ and $W_4/\|\mathbf{B}\|^2$ in energy bounds (26), (41) and (56), respectively. The dotted vertical line indicates the time shown in Figure 5.

could be computed (with care) for arbitrary distributions, including those from the numerical simulations in Section 5. This could provide a normalized way to assess how “helical” is a given magnetic configuration in the solar corona, with possible application to predicting solar eruptions.

What about domains other than spherical shells? Firstly, we expect all of our results to extend (with small modification) to the case of an infinite plane slab (the volume between two parallel planes), since the poloidal-toroidal decomposition of \mathbf{B} also exists there. We omit this here since such a domain is of limited practical relevance in solar physics. More relevant would be a finite domain, such as a Cartesian box. For such a domain, Démoulin (2007) notes that we can again write $H_R = \int_V \mathbf{A}^c \cdot \mathbf{B} dV$, by choosing \mathbf{A}^c to match $\mathbf{n} \times \mathbf{A}^c = \mathbf{n} \times \mathbf{A}_p^c$ on ∂V , where the reference vector potential \mathbf{A}_p^c satisfies the Coulomb gauge conditions $\nabla \cdot \mathbf{A}_p^c = 0$ throughout V and $\mathbf{n} \cdot \mathbf{A}_p^c|_{\partial V} = 0$. However, except for spherical shells or infinite slabs, this does not yield an explicit expression for \mathbf{A}^c in terms of \mathbf{B} , so that it is unclear how to derive an energy bound for $\|\mathbf{B}\|^2$, although MacTaggart (2025) has recently derived a free energy bound similar to Section 3.2.

In certain other cases – for example, a doubly-periodic domain (Xiao et al. 2025), or a finite flux tube (Prior & Yeates 2014; Candelaresi et al. 2021) – there are known \mathbf{A} with explicit expressions in terms of \mathbf{B} and associated interpretations of the corresponding H in terms of winding numbers. However, in these cases, H can differ from H_R (an explicit example is given by Prior & Yeates 2014). This raises the question whether H_R is the most physically relevant helicity definition in general, or whether it coincides with such a definition only in more specialized domains such as spherical shells. Indeed, MacTaggart & Valli (2023) have proposed how to extend H_R to multiply-connected domains, but the relation to energy warrants further investigation.

ARY was supported by UKRI/STFC grant UKRI1216. The authors thank Christopher Prior for comments on an initial draft, as well as Daining Xiao and Mitchell Berger for fruitful discussions. The SDO data are courtesy of NASA and the SDO/HMI science team.

Facility: SDO (HMI)

APPENDIX

A. PROOF OF POINCARÉ INEQUALITY

To derive (24) for \mathbf{A}_p^* , we adapt an argument of [Cantarella et al. \(2001\)](#) which was applied originally to the Biot-Savart integral in a magnetically closed domain. We start from the expression (17) for \mathbf{A}^* , using (18) to write it in the form

$$\mathbf{A}^*(\mathbf{x}) = \frac{1}{4\pi r^3} \int_{S'_r} \left[B_r(\mathbf{x}') \frac{\mathbf{x}' \times \mathbf{x}}{1 - \cos \xi} + \frac{\mathbf{B}(\mathbf{x}') \cdot (\mathbf{x} \times \mathbf{x}')}{1 - \cos \xi} \mathbf{e}_r \right] dS'. \quad (\text{A1})$$

Since $\mathbf{x} = r\mathbf{e}_r$, the two terms in the integrand are orthogonal vectors for any \mathbf{x}' , so

$$|\mathbf{A}^*(\mathbf{x})|^2 = \frac{1}{(4\pi r^3)^2} \left[\left| \int_{S'_r} B_r(\mathbf{x}') \frac{\mathbf{x}' \times \mathbf{x}}{1 - \cos \xi} dS' \right|^2 + \left| \int_{S'_r} \frac{\mathbf{B}(\mathbf{x}') \cdot (\mathbf{x} \times \mathbf{x}')}{1 - \cos \xi} dS' \right|^2 \right]. \quad (\text{A2})$$

The first term in (A2) satisfies

$$\left| \int_{S'_r} B_r(\mathbf{x}') \frac{\mathbf{x}' \times \mathbf{x}}{1 - \cos \xi} dS' \right| \leq \int_{S'_r} \left| B_r(\mathbf{x}') \right| \frac{|\mathbf{x}' \times \mathbf{x}|^{1/2}}{(1 - \cos \xi)^{1/2}} \left| \frac{|\mathbf{x}' \times \mathbf{x}|^{1/2}}{(1 - \cos \xi)^{1/2}} dS' \right| \quad (\text{A3})$$

$$\leq r^2 \left(\int_{S'_r} |B_r(\mathbf{x}')|^2 \Gamma(\xi) dS' \right)^{1/2} \left(\int_{S'_r} \Gamma(\xi) dS' \right)^{1/2}. \quad (\text{A4})$$

using Cauchy-Schwartz and the fact that $|\mathbf{x}' \times \mathbf{x}| = r^2 \sin \xi$. As in (20), we use the shorthand $\Gamma(\xi) = \sin \xi / (1 - \cos \xi)$. Similarly the second term in (A2) satisfies

$$\left| \int_{S'_r} \frac{\mathbf{B}(\mathbf{x}') \cdot (\mathbf{x} \times \mathbf{x}')}{1 - \cos \xi} dS' \right| \leq r^2 \left(\int_{S'_r} |\mathbf{B}_h(\mathbf{x}')|^2 \Gamma(\xi) dS' \right)^{1/2} \left(\int_{S'_r} \Gamma(\xi) dS' \right)^{1/2}. \quad (\text{A5})$$

By symmetry, the integral $\int_{S'_r} \Gamma(\xi) dS'$ must be independent of \mathbf{x} , so can be directly evaluated by setting \mathbf{x} to be the north pole, giving

$$\int_{S'_r} \Gamma(\xi) dS' = 2\pi^2 r^2. \quad (\text{A6})$$

So overall (A2) gives

$$|\mathbf{A}^*(\mathbf{x})|^2 \leq \frac{1}{8} \int_{S'_r} |\mathbf{B}(\mathbf{x}')|^2 \Gamma(\xi) dS'. \quad (\text{A7})$$

Integrating over all \mathbf{x} in S_r then gives

$$\int_{S_r} |\mathbf{A}^*(\mathbf{x})|^2 dS \leq \frac{1}{8} \int_{S'_r} |\mathbf{B}(\mathbf{x}')|^2 \left(\int_{S_r} \Gamma(\xi) dS \right) dS' = \frac{\pi^2 r^2}{4} \int_{S'_r} |\mathbf{B}(\mathbf{x}')|^2 dS'. \quad (\text{A8})$$

Finally, integrating over r gives

$$\|\mathbf{A}^*(\mathbf{x})\|^2 \leq \int_{r_0}^{r_1} \frac{\pi^2 r^2}{4} \int_{S_r} |\mathbf{B}(\mathbf{x}')|^2 dS' dr \leq \frac{\pi^2 r_1^2}{4} \|\mathbf{B}(\mathbf{x})\|^2. \quad (\text{A9})$$

B. WOLTJER'S THEOREM FOR RELATIVE HELICITY

[Berger \(1984\)](#) (in Appendix A) showed that the celebrated theorem of [Woltjer \(1958\)](#) applies equally to relative helicity: namely, the minimum energy state (if it exists) for a specified H_R and $\mathbf{B} \cdot \mathbf{n}|_{\partial V}$ must be a linear force-free field satisfying (27). Here we use (13) to give a simple alternative proof for our spherical shell domain.

Start by considering the first variation of $\|\mathbf{B}\|^2$. Integration by parts gives

$$\delta \|\mathbf{B}\|^2 = 2 \int_V \delta \mathbf{A}^* \cdot (\nabla \times \mathbf{B}) dV - 2 \oint_{\partial V} \mathbf{B} \cdot (\delta \mathbf{A}^* \times \mathbf{n}) dS. \quad (\text{B10})$$

The surface term vanishes since $\delta\mathbf{A}^* \times \mathbf{n} = \mathbf{0}$, because $\mathbf{A}^* \times \mathbf{n}|_{\partial V}$ in the poloidal-toroidal gauge (5) depends only on $B_r|_{\partial V}$, which is fixed by assumption. On the other hand, and applying a similar boundary condition, we find

$$\delta H_R = 2 \int_V \delta\mathbf{A}^* \cdot \mathbf{B} dV. \quad (\text{B11})$$

We then follow the original argument of Woltjer (1958) to minimize $\|\mathbf{B}\|^2$ with fixed H_R and fixed B_r on the boundaries, introducing a Lagrange multiplier α to obtain

$$\int_V 2\delta\mathbf{A}^* \cdot (\nabla \times \mathbf{B} - \alpha\mathbf{B}) dV = 0. \quad (\text{B12})$$

This holds for all allowable perturbations $\delta\mathbf{A}^*$ if and only if (27) is satisfied.

C. DIPOLAR LINEAR FORCE-FREE EXAMPLE

By separation of variables (e.g., Berger 1985; Durrant 1989), it may be shown that a solution to (27) with B_r matching (28) on S_0 and S_1 takes the form

$$\mathbf{B} = B_0 \left[\frac{2R \cos \theta}{r} \mathbf{e}_r - \frac{(rR)' \sin \theta}{r} \mathbf{e}_\theta + \alpha R \sin \theta \mathbf{e}_\phi \right], \quad (\text{C13})$$

where the prime denotes differentiation with respect to r , and the radial function $R(r)$ is given in terms of spherical Bessel functions as

$$R(r) = A j_1(\alpha r) + B y_1(\alpha r), \quad (\text{C14})$$

with constants A, B determined by the boundary conditions on S_0 and S_1 . Specifically,

$$A = -\frac{r_0 y_1(\alpha r_1) - c r_1 y_1(\alpha r_0)}{2\lambda}, \quad B = \frac{r_0 j_1(\alpha r_1) - c r_1 j_1(\alpha r_0)}{2\lambda}, \quad (\text{C15})$$

where we have used the shorthand

$$\lambda \equiv y_1(\alpha r_0) j_1(\alpha r_1) - j_1(\alpha r_0) y_1(\alpha r_1), \quad c \equiv \frac{3r_0^3}{r_0^3 + 2r_1^3}. \quad (\text{C16})$$

This solution exists for every value of $\alpha \in \mathbb{R}$ except for the discrete set of ‘‘resonant’’ values where $\lambda = 0$ (Berger 1985). These correspond to the values of α for which the homogeneous problem with $B_r(r_0, \theta, \phi) = B_r(r_1, \theta, \phi) = 0$ has a non-trivial solution – the curl eigenfunctions in a spherical shell (Cantarella et al. 2000). The lowest of these resonant α values for each r_0 is indicated by a dashed vertical line in Figure 2(a).

For a linear force-free field, we have $\mathbf{e}_r \cdot \nabla \times \mathbf{B} = \alpha B_r$, so since $\cos \theta$ is an eigenfunction of ∇_h^2 , the solutions to (6) and (7) are

$$P(r, \theta) = B_0 r R \cos \theta, \quad T(r, \theta) = \alpha P(r, \theta), \quad (\text{C17})$$

with resulting vector potential

$$\mathbf{A}^* = B_0 [\alpha r R \cos \theta \mathbf{e}_r + R \sin \theta \mathbf{e}_\phi]. \quad (\text{C18})$$

By (13), the relative helicity (cf. Berger 1985) is therefore

$$H_R = \int_V \mathbf{A}^* \cdot \mathbf{B} dV = \frac{16\pi B_0^2 \alpha}{3} \int_{r_0}^{r_1} (rR)^2 dr. \quad (\text{C19})$$

Similarly the energy reduces to the single integral

$$\|\mathbf{B}\|^2 = \frac{8\pi B_0^2}{3} \int_{r_0}^{r_1} [(2 + \alpha^2 r^2) R^2 + ([rR]')^2] dr. \quad (\text{C20})$$

At the resonant values of α , both $\|\mathbf{B}\|^2$ and H_R diverge to infinity, although their ratio – as shown in Figure 2(a) – does not, because the factor of λ^{-2} cancels between them.

To compute H_J and H_{PJ} , it is convenient to use the vector potential

$$\mathbf{A}_p = \frac{B_0 r_0^3 (r^3 + 2r_1^3)}{2r^2(r_0^3 + 2r_1^3)} \sin \theta \mathbf{e}_\phi \quad (C21)$$

for the reference field (28), since in this gauge $\mathbf{A}_p \cdot \mathbf{B}_p = 0$ and we have

$$H_{PJ} = 2 \int_V \mathbf{A}_p \cdot \mathbf{B} dV = \frac{8\pi B_0^2 r_0^3 \alpha}{3(r_0^3 + 2r_1^3)} \int_{r_0}^{r_1} (r^3 + 2r_1^3) R dr, \quad (C22)$$

from which we compute H_J using $H_J = H_R - H_{PJ}$.

Finally, note that the field line helicity \mathcal{A} in these fields has the same sign for every field line. This follows from (51) noting that

$$\mathbf{A}^* \cdot \mathbf{B} = \alpha B_0^2 R^2 (1 + \cos^2 \theta). \quad (C23)$$

D. NUMERICAL METHOD FOR FIELD LINE HELICITY

As with all calculations of magnetic helicity, care is needed to use a numerical method that does not introduce spurious $\nabla \cdot \mathbf{B}$ contributions (Valori et al. 2016). Here we summarize how the calculations of \mathcal{A} and hence \bar{H} in Section 5 were made (code available at Yeates 2025). As indicated by Yeates (2024), the simulations use a finite-volume method and provide \mathbf{B} components on the corresponding cell faces of a staggered mesh. Since neighboring cells share the face values, this ensures that $\nabla \cdot \mathbf{B} = 0$ is preserved in an integrated sense within each three-dimensional grid cell. To ensure that $\nabla \times \mathbf{A} = \mathbf{B}$ when computing \mathbf{A} , the components of \mathbf{A} are staggered on the cell edges, and computed in such a way as to enforce the discrete Stokes Theorem, $\int_{S_{ij}} \mathbf{n} \cdot \mathbf{B} dS = \oint_{\partial S_{ij}} \mathbf{A} \cdot d\mathbf{l}$ on every cell face S_{ij} .

D.1. Vector potential

Rather than computing \mathcal{A} directly from \mathbf{A}^* using (52), we instead evaluate

$$\mathcal{A}(L_i) = \int_{L_i} \mathbf{A}' \cdot d\mathbf{l} \quad (D24)$$

where \mathbf{A}' is simpler to compute. To ensure that \mathcal{A} is unmodified for all field lines by this gauge transformation, we impose that (i) $\mathbf{e}_r \times \mathbf{A}' = \mathbf{e}_r \times \mathbf{A}^*$ on both S_0 and S_1 , and (ii) $\oint_{S_r} A'_r dS = 0$ on every S_r for $r \in [r_0, r_1]$. See this by writing $\mathbf{A}' = \mathbf{A}^* + \nabla \chi$, so that condition (i) implies that $\chi(r_0, \theta, \phi) \equiv \chi_0$ and $\chi(r_1, \theta, \phi) \equiv \chi_1$, both constant. Thus

$$\int_{L_i} \mathbf{A}' \cdot d\mathbf{l} = \mathcal{A}(L_i) + \chi_1 - \chi_0. \quad (D25)$$

Then, noting from (9) that $\oint_{S_r} A_r^* dS = 0$, condition (ii) implies that

$$\oint_{S_r} \frac{\partial \chi}{\partial r} dS = 0 \implies \frac{d}{dr} \left(\frac{1}{r^2} \oint_{S_r} \chi dS \right) = 0 \implies \chi_1 = \chi_0. \quad (D26)$$

D.2. Numerical algorithm

To compute a suitable \mathbf{A}' , we proceed as follows:

1. Compute \mathbf{A}^\dagger in the DeVore-Coulomb gauge (DeVore 2000; Moraitis et al. 2018),

$$\mathbf{A}^\dagger(r, \theta, \phi) = \frac{r_0}{r} \nabla \times [\psi(\theta, \phi) \mathbf{e}_r] + \frac{1}{r} \int_{r_0}^r \mathbf{B}(r', \theta, \phi) \times \mathbf{e}_r r' dr', \quad \text{where } \nabla_h^2 \psi = -B_r(r_0, \theta, \phi), \quad (D27)$$

choosing the solution ψ with zero mean over S_1 . By definition, $A_r^\dagger \equiv 0$ so \mathbf{A}^\dagger already satisfies condition (ii). In addition, ψ coincides with P from Section 2, so \mathbf{A}^\dagger also satisfies condition (i) on S_0 , but not (necessarily) on S_1 . Both the Poisson equation and the radial integral are discretized so that the discrete Stokes Theorem is satisfied on each cell face, with ψ co-located with B_r on the radial cell faces.

2. Change gauge to $\mathbf{A}' = \mathbf{A}^\dagger + \nabla g$ satisfying both conditions (i) and (ii), while preserving $\oint_{\partial S_{ij}} \mathbf{A}' \cdot d\mathbf{l} = \oint_{\partial S_{ij}} \mathbf{A}^\dagger \cdot d\mathbf{l}$ on every cell face. The gauge function g is located at cell vertices, and determined as follows:

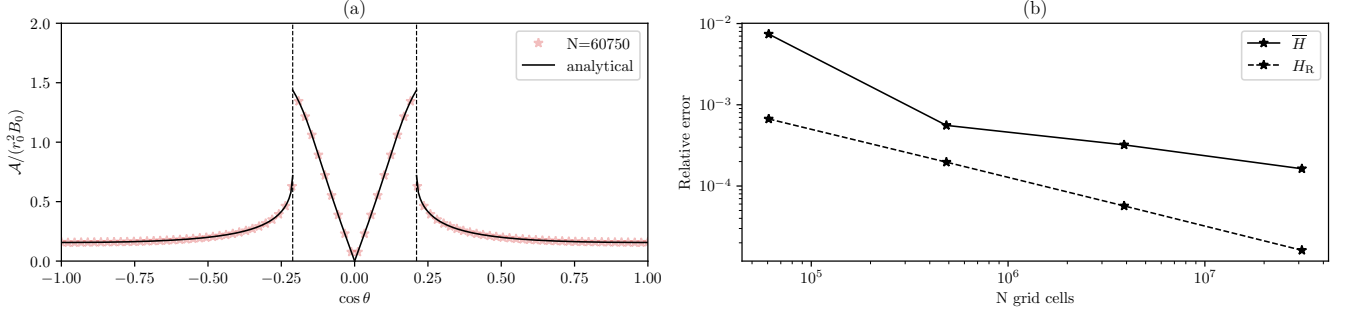


Figure 7. Numerical convergence test using the linear force-free field (C13). Panel (a) shows \mathcal{A} as a function of footpoint colatitude on S_0 , while panel (b) shows how the errors in numerically-approximated \bar{H} and H_R depend on the mesh resolution for discretizing \mathbf{B} .

- Compute the polar values $A_\theta^*(r_1, 0, \phi)$ and $A_\theta^*(r_1, \pi, \phi)$ on S_1 by solving $\nabla_h^2 P = -B_r$. These will be used as a boundary conditions in the next step.
- Compute the gauge function $g(r_1, \theta, \phi)$ on S_1 by solving $\nabla_h^2 g = -\nabla_h \cdot \mathbf{A}^\dagger$ on S_1 , choosing the solution with zero mean (this additive constant affects only A'_r , not A'_θ or A'_ϕ). This will ensure that $\nabla_h \cdot \mathbf{A}' = 0$ on S_1 , and hence that $\mathbf{e}_r \times \mathbf{A}' = \mathbf{e}_r \times \mathbf{A}^*$ on S_1 . Since the first and last rows of vertices are at the poles, we avoid numerical problems by solving for g with these two rows omitted, setting the values of g at the poles with the Neumann condition $\partial g / \partial \theta = A_\theta^* - A_\theta^\dagger$.
- Set $g(r_0, \theta, \phi) \equiv 0$ so as to preserve condition (i) on S_0 .
- Fill in $g(r, \theta, \phi)$ for intermediate S_r by linear interpolation between $g(r_0, \theta, \phi) \equiv 0$ and $g(r_1, \theta, \phi)$. This will preserve condition (ii) since $g(r_1, \theta, \phi)$ has zero mean.

Once \mathbf{A}' has been computed, we trace field lines L_i using the (second-order) midpoint method, then evaluate (D24) by numerical integration of \mathbf{A}' along each field line. To compute \bar{H} , we assume that there are no closed field lines and approximate (54) by tracing field lines from grids at twice the original mesh resolution on both S_0 and S_1 .

D.3. Convergence test

Figure 7 demonstrates convergence of the numerical scheme, for a test where the linear force-free field (C13) is discretized on the same three-dimensional mesh used for the simulations in Section 5. We fix $r_0 = 0.8$, $r_1 = 1$, $\alpha = 1.6$ and $B_0 = 1$. For (C13), \mathcal{A} may be calculated to arbitrary precision by parameterizing (52) with the radial component r , and evaluating an integral in r for each field line. This ‘‘analytical’’ solution is shown by the solid curve in Figure 7(a); note the separatrices at

$$\cos \theta = \pm \sqrt{1 - \frac{r_1 R(r_1)}{r_0 R(r_0)}}, \quad (\text{D28})$$

between open field lines nearer the poles and closed field lines nearer the equator. The star symbols show the \mathcal{A} profile computed entirely ‘‘agnostically’’ from the discretized datacube using the method described in Section D.2. In this case, the datacube resolution was only $15 \times 45 \times 90$ (a quarter of that used in the numerical simulations in Section 5).

The solid line in Figure 7(b) shows the error in \bar{H} when numerically computed from the datacube at resolutions from $15 \times 45 \times 90$ up to $120 \times 360 \times 720$. The ground truth for this test is given by (C19) since $\bar{H} = H_R$ for (C13). Despite the multiple stages in the numerical calculation (discretizing \mathbf{B} on the mesh, computing \mathbf{A}' , tracing field lines, integrating \mathcal{A} along them, and integrating the results over S_0 and S_1), we observe (modest) convergence with the mesh resolution. The dashed line shows the approximation of H_R by direct numerical integration of $\mathbf{A}' \cdot \mathbf{B}$ on the three-dimensional mesh, which avoids several of these stages and is somewhat more accurate, but cannot be used to compute \bar{H} when \mathcal{A} has mixed signs.

REFERENCES

Aly, J. J. 2014, in Journal of Physics Conference Series, Vol. 544, Journal of Physics Conference Series (IOP), 012003, doi: [10.1088/1742-6596/544/1/012003](https://doi.org/10.1088/1742-6596/544/1/012003)

Arnol'd, V. I. 1986, Sel. Math. Sov., 5, 327

Backus, G. 1958, *Annals of Physics*, 4, 372, doi: [10.1016/0003-4916\(58\)90054-X](https://doi.org/10.1016/0003-4916(58)90054-X)

Berger, M. A. 1984, *Geophysical and Astrophysical Fluid Dynamics*, 30, 79, doi: [10.1080/03091928408210078](https://doi.org/10.1080/03091928408210078)

—. 1985, *ApJS*, 59, 433, doi: [10.1086/191079](https://doi.org/10.1086/191079)

—. 1988, *A&A*, 201, 355

—. 1993, *PhRvL*, 70, 705, doi: [10.1103/PhysRevLett.70.705](https://doi.org/10.1103/PhysRevLett.70.705)

—. 1999, *Plasma Physics and Controlled Fusion*, 41, B167, doi: [10.1088/0741-3335/41/12B/312](https://doi.org/10.1088/0741-3335/41/12B/312)

—. 2003, in *Advances in Nonlinear Dynamics*, ed. A. Ferriz-Mas & M. Núñez, 345–374, doi: [10.1201/9780203493137.ch10](https://doi.org/10.1201/9780203493137.ch10)

Berger, M. A., & Field, G. B. 1984, *Journal of Fluid Mechanics*, 147, 133, doi: [10.1017/S0022112084002019](https://doi.org/10.1017/S0022112084002019)

Berger, M. A., & Hornig, G. 2018, *Journal of Physics A Mathematical General*, 51, 495501, doi: [10.1088/1751-8121/aaea88](https://doi.org/10.1088/1751-8121/aaea88)

Blackman, E. G. 2015, *SSRv*, 188, 59, doi: [10.1007/s11214-014-0038-6](https://doi.org/10.1007/s11214-014-0038-6)

Bobra, M. G., Sun, X., Hoeksema, J. T., et al. 2014, *SoPh*, 289, 3549, doi: [10.1007/s11207-014-0529-3](https://doi.org/10.1007/s11207-014-0529-3)

Candelaresi, S., & Brandenburg, A. 2011, *PhRvE*, 84, 016406, doi: [10.1103/PhysRevE.84.016406](https://doi.org/10.1103/PhysRevE.84.016406)

Candelaresi, S., Hornig, G., MacTaggart, D., & Simitev, R. 2021, *Commun Nonlinear Sci Numer Simulat*, 103, 106015, doi: [10.1016/j.cnsns.2021.106015](https://doi.org/10.1016/j.cnsns.2021.106015)

Cantarella, J., DeTurck, D., & Gluck, H. 2001, in *Proceedings of the Conference in Honor of the 70th Birthday of Joan Birman*, ed. J. Gilman, X.-S. Lin, & W. Menasco (Providence, RI: Americal Mathematical Society/International Press), 1–22

Cantarella, J., DeTurck, D., Gluck, H., & Teytel, M. 2000, *Physics of Plasmas*, 7, 2766, doi: [10.1063/1.874127](https://doi.org/10.1063/1.874127)

Démoulin, P. 2007, *Advances in Space Research*, 39, 1674, doi: [10.1016/j.asr.2006.12.037](https://doi.org/10.1016/j.asr.2006.12.037)

Démoulin, P., & Pariat, E. 2009, *Advances in Space Research*, 43, 1013, doi: [10.1016/j.asr.2008.12.004](https://doi.org/10.1016/j.asr.2008.12.004)

Demoulin, P., Pariat, E., & Berger, M. A. 2006, *SoPh*, 233, 3, doi: [10.1007/s11207-006-0010-z](https://doi.org/10.1007/s11207-006-0010-z)

DeVore, C. R. 2000, *ApJ*, 539, 944, doi: [10.1086/309274](https://doi.org/10.1086/309274)

Durrant, C. J. 1989, *Australian Journal of Physics*, 42, 317, doi: [10.1071/PH890317](https://doi.org/10.1071/PH890317)

Finn, J. M., & Antonson, Jr., T. M. 1985, *Comments on Plasma Physics and Controlled Fusion*, 9, 111

Freedman, M. H., & He, Z.-X. 1991, *Annals of Mathematics*, 134, 189

Linan, L., Pariat, É., Moraitis, K., Valori, G., & Leake, J. 2018, *ApJ*, 865, 52, doi: [10.3847/1538-4357/aadae7](https://doi.org/10.3847/1538-4357/aadae7)

MacTaggart, D. 2025, *Discover Space*, 129, 19, doi: [10.1007/s11038-025-09578-8](https://doi.org/10.1007/s11038-025-09578-8)

MacTaggart, D., & Valli, A. 2023, *Journal of Physics A Mathematical General*, 56, 435701, doi: [10.1088/1751-8121/acfd6c](https://doi.org/10.1088/1751-8121/acfd6c)

Martin, S. F. 1998, *SoPh*, 182, 107, doi: [10.1023/A:1005026814076](https://doi.org/10.1023/A:1005026814076)

Matthaeus, W. H., & Goldstein, M. L. 1982, *J. Geophys. Res.*, 87, 6011, doi: [10.1029/JA087iA08p06011](https://doi.org/10.1029/JA087iA08p06011)

Moffatt, H. K., & Dormy, E. 2019, *Self-Exciting Fluid Dynamos*, doi: [10.1017/9781107588691](https://doi.org/10.1017/9781107588691)

Moffatt, H. K., & Ricca, R. L. 1992, *Proceedings of the Royal Society of London Series A*, 439, 411, doi: [10.1098/rspa.1992.0159](https://doi.org/10.1098/rspa.1992.0159)

Moraitis, K., Pariat, É., Savcheva, A., & Valori, G. 2018, *SoPh*, 293, 92, doi: [10.1007/s11207-018-1314-5](https://doi.org/10.1007/s11207-018-1314-5)

Narita, Y. 2024, in *Helicities in Geophysics, Astrophysics, and Beyond*, ed. K. Kuzanyan, N. Yokoi, M. K. Georgoulis, & R. Stepanov, Vol. 283, 105–116, doi: [10.1002/978119841715.ch7](https://doi.org/10.1002/978119841715.ch7)

Pevtsov, A. A., & Balasubramaniam, K. S. 2003, *Advances in Space Research*, 32, 1867, doi: [10.1016/S0273-1177\(03\)90620-X](https://doi.org/10.1016/S0273-1177(03)90620-X)

Pevtsov, A. A., Berger, M. A., Nindos, A., Norton, A. A., & van Driel-Gesztelyi, L. 2014, *SSRv*, 186, 285, doi: [10.1007/s11214-014-0082-2](https://doi.org/10.1007/s11214-014-0082-2)

Pontin, D. I., Candelaresi, S., Russell, A. J. B., & Hornig, G. 2016, *Plasma Physics and Controlled Fusion*, 58, 054008, doi: [10.1088/0741-3335/58/5/054008](https://doi.org/10.1088/0741-3335/58/5/054008)

Prior, C., & Yeates, A. R. 2014, *ApJ*, 787, 100, doi: [10.1088/0004-637X/787/2/100](https://doi.org/10.1088/0004-637X/787/2/100)

Ricca, R. L. 2013, *Geophysical and Astrophysical Fluid Dynamics*, 107, 385, doi: [10.1080/03091929.2012.681782](https://doi.org/10.1080/03091929.2012.681782)

Schuck, P. W., & Linton, M. G. 2024, *ApJ*, 961, 156, doi: [10.3847/1538-4357/acf471](https://doi.org/10.3847/1538-4357/acf471)

Thalmann, J. K., Georgoulis, M. K., Liu, Y., et al. 2021, *ApJ*, 922, 41, doi: [10.3847/1538-4357/ac1f93](https://doi.org/10.3847/1538-4357/ac1f93)

Toriumi, S., & Wang, H. 2019, *Living Reviews in Solar Physics*, 16, 3, doi: [10.1007/s41116-019-0019-7](https://doi.org/10.1007/s41116-019-0019-7)

Valori, G., Démoulin, P., Pariat, E., et al. 2020, *A&A*, 643, A26, doi: [10.1051/0004-6361/202038533](https://doi.org/10.1051/0004-6361/202038533)

Valori, G., Pariat, E., Anfinogentov, S., et al. 2016, *SSRv*, 201, 147, doi: [10.1007/s11214-016-0299-3](https://doi.org/10.1007/s11214-016-0299-3)

Woltjer, L. 1958, *Proceedings of the National Academy of Science*, 44, 489, doi: [10.1073/pnas.44.6.489](https://doi.org/10.1073/pnas.44.6.489)

Xiao, D., Prior, C. B., & Yeates, A. R. 2023, *Journal of Physics A Mathematical General*, 56, 205201, doi: [10.1088/1751-8121/accc17](https://doi.org/10.1088/1751-8121/accc17)

—. 2025, *Proceedings of the Royal Society of London Series A*, 481, 20240152, doi: [10.1098/rspa.2024.0152](https://doi.org/10.1098/rspa.2024.0152)

Yeates, A. R. 2020, ApJL, 898, L49,
doi: [10.3847/2041-8213/aba762](https://doi.org/10.3847/2041-8213/aba762)

—. 2024, SoPh, 299, 83, doi: [10.1007/s11207-024-02328-5](https://doi.org/10.1007/s11207-024-02328-5)

—. 2025, sphtools, v1.0, Zenodo,
doi: [10.5281/zenodo.17607526](https://doi.org/10.5281/zenodo.17607526)

Yeates, A. R., & Berger, M. A. 2024, in *Helicities in Geophysics, Astrophysics, and Beyond*, ed. K. Kuzanyan, N. Yokoi, M. K. Georgoulis, & R. Stepanov, Vol. 283, 1–16, doi: [10.1002/9781119841715.ch1](https://doi.org/10.1002/9781119841715.ch1)

Yeates, A. R., Bianchi, F., Welsch, B. T., & Bushby, P. J. 2014, A&A, 564, A131,
doi: [10.1051/0004-6361/201323276](https://doi.org/10.1051/0004-6361/201323276)

Yeates, A. R., & Hornig, G. 2016, A&A, 594, A98,
doi: [10.1051/0004-6361/201629122](https://doi.org/10.1051/0004-6361/201629122)

Yeates, A. R., Amari, T., Contopoulos, I., et al. 2018, SSRv, 214, 99, doi: [10.1007/s11214-018-0534-1](https://doi.org/10.1007/s11214-018-0534-1)

Yi, S., & Choe, G. S. 2022, Scientific Reports, 12, 2944,
doi: [10.1038/s41598-022-07040-7](https://doi.org/10.1038/s41598-022-07040-7)

Yoshida, Z., & Giga, Y. 1990, Math. Z., 204, 235